Supporting Information

Balancing Polysulfide Containment and Energy Loss in Lithium–Sulfur Batteries

Borui Liu,[†,⊥] Huimin Gu,[‡,⊥] Juan F. Torres,[§] Zongyou Yin[*,‡] and Antonio Tricoli[*,†,‡]

† Nanotechnology Research Laboratory, Faculty of Engineering, University of Sydney, Darlington, New South Wales, 2008 Australia

‡ Research School of Chemistry, Australian National University, Canberra, Australian Capital Territory, 2601 Australia

§ School of Engineering, College of Engineering and Computer Science, Australian National University, Canberra, ACT, 2601 Australia

[⊥] These authors contributed equally to this work.

* Corresponding author.

E-mail: antonio.tricoli@sydney.edu.au, zongyou.yin@anu.edu.au

Experimental Methods

1. Material synthesis

Synthesis of GO and rGO: Graphene oxide (GO) and reduced graphene oxide (rGO) were synthesized according to a previously reported method.[1] First, natural graphite was chemically oxidized using a modified Hummers' method to obtain GO. To prepare rGO, 30 mg of GO powder was ultrasonically dispersed in 50 mL of anhydrous ethylene glycol (EG, 99.8%) for at least 1 hour. The dispersion was then vigorously stirred at 180°C for 3 hours in a reflux reactor. The final rGO nanosheets were purified in ethanol and DI water and dried by lyophilization.

Synthesis of HG: Nanoscale holes were created on graphene nanosheets using solid-state etching by oxidative nanoparticles. For instance, to synthesize 030HG nanosheets, 60 mg of as-prepared GO powder and 74.7 mg (0.30 mmol) $(CH_3COO)_2Co{\cdot}4H_2O$ (≥98.0%) were added in 100 mL of anhydrous ethylene glycol (EG, 99.8%) and ultrasonicated for at least 1 hour. The mixture was vigorously stirred at 180°C for 3 hours in a reflux reactor to form a thin layer of cobalt compound precursor on graphene nanosheets (Co-pre/G, **Figure S11**). The Co-precursor/G nanosheets were purified in ethanol and DI water and dried by lyophilization. Subsequently, the Co-pre/G nanosheets were annealed at 800°C for 1 hour in N_2 flow to form Co metallic nanoparticles on graphene nanosheets (CoNP/G, **Figure S12**). The CoNP/G nanosheets were further annealed at 200°C for 2 hours in air to form partially oxidized Co_3O_4-Co nanoparticles on graphene nanosheets (Co_3O_4-CoNP/G). Next, the Co_3O_4-CoNP/G nanosheets were re-annealed at 800°C for 1 hour in N_2 flow, during which the Co_3O_4 in-situ etched nanoscale holes on the graphene to form CoNPs/HG (**Figure S13**) nanosheets. The final 030HG nanosheets (**Figure S14**) were obtained by soaking the Co_3O_4/HG nanosheets in 8.0M HCl solution at 60°C overnight. To synthesize the 050HG nanosheets, $(CH_3COO)_2Co{\cdot}4H_2O$ was increased to 124.5 mg (0.50 mmol) in the above process, while keeping other parameters unchanged.

Synthesis of $Co(OH)_2$: $Co(NO_3)_2{\cdot}6H_2O$ (291 mg, 1 mmol, ≥98%) was dissolved in 100 mL of a mixture of methanol/DI H_2O (1:1, v/v) to form solution A. Ammonium hydroxide solution (NH_4OH, 28.0-30.0% NH_3 basis, 150 μL) was diluted in 50 mL of a mixture of methanol/DI H_2O (1:1, v/v) to form solution B. Solutions A and B were kept at 4°C in an ice-water bath, and then solution B was added dropwise into solution A under magnetic stirring at 1000 rpm. The reaction was maintained at 4°C for 30 minutes until a homogeneous greenish $Co(OH)_2$ colloidal solution formed. The resulting $Co(OH)_2$ powder was purified and collected by centrifugation in DI water multiple times and then dried by lyophilization.

Synthesis of SnS_2: First, 351 mg $SnCl_4$ (1 mmol, ≥98%) and 150 mg ethanethioamide (2 mmol, ≥99.0%) were thoroughly mixed in 100 mL ethanol. The reaction was kept under magnetic stirring for 30 min at 4°C in an ice-water bath. Then, the solution was ultrasonicated for 30 min until a homogeneous brownish SnS_2 colloidal solution was formed. The resulting SnS_2 powder was purified and collected by centrifugation in ethanol and DI H_2O multiple times, and then dried by lyophilization.

2. Fabrication of modified membranes

Here, the membrane is defined as the micro/meso-porous coating layer, while the "membrane-modified separator" or "modified separator" is defined as the structure comprising of the

micro/meso-porous coating layer applied over the commercial PP separator (1x membrane + 1x PP). The membrane-modified separators were fabricated using a simple filtration process. A commercial PP separator (Celgard 2400, thickness 25 μm) was selected as the base material for coating the membranes, and it served as the filter paper during the fabrication process. The following materials were chosen for constructing membranes: rGO, GO, $Co(OH)_2$, SnS_2, MoS_2, 030HG, and 050HG. To prepare the coating dispersions, 10 mg of rGO, 030HG, or 050HG was added to 50 mL of anhydrous 1-Methyl-2-pyrrolidone (NMP, 99.5%), while 10 mg of GO, $Co(OH)_2$, SnS_2, or 10 mL of MoS_2 suspension (consisting of LiOH-stabilized few-layer MoS_2 nanosheets dispersed in ethanol/H_2O, with C_{MoS2} = 1 mg mL^{-1} and d_{MoS2} = 0.02-1 μm, Sigma) was added to 50 mL of DI water. The resulting mixtures were ultrasonicated for 12 hours to achieve a homogeneous dispersion.

To ensure a uniform membrane coating in all modified separators, the dispersions were slowly added to a 500 mL open bottle (d = 84 mm) of a filtering flask. The filtering flask was left undisturbed until the filtration process was complete. After filtration, the modified separators were dried at 50°C overnight before use. The mass of membranes coated on PP separators was approximately 0.18 mg cm^{-2}. For comparison, a thinner version of the GO membrane was also fabricated, with a loading of approximately 0.09 mg cm^{-2}.

3. Material characterizations

The SEM analysis was performed using a Zeiss UltraPlus analytical FESEM at 3 kV. XRD measurements were conducted using a Bruker system (D2 Phaser) equipped with Cu Kα radiation, with an average wavelength of 1.54059 Å. The thicknesses of the membranes were determined using a Starrett 3732 digital thickness gauge with a resolution of 0.001 mm, and the differences in thickness between a bare PP separator and the modified separators were illustrated in **Figure S7**.

4. Derivation of capacity output and energy output *vs* overpotential

To conceptually illustrate the impact of overpotential, as induced by the membranes, on the charging/discharging plateaus of Li–S batteries, charging/discharging profiles of a model Li–S coin cell battery are needed as the theoretical reference. The model Li–S coin cell battery consists of a lithium metal anode, a sulfur cathode, and a 40 μL electrolyte containing 1M LiTFSI and 0.2 M $LiNO_3$ in DOL/DME (1:1, v/v), along with a layer of commercial polypropylene (PP) separator. The sulfur cathode features a sulfur mass loading of 0.1 mg cm^{-2}, including 5wt% LA133 binder and 20wt% carbon black. Experimental testing was conducted at 0.1C, and the charge-discharge data from the third cycle were utilized. The red and blue solid lines in **Figure 2a** represent the maximum values of specific capacity, denoting 100% sulfur utilization.

To derive the discharge capacity output and energy output curves in **Figure 2b**, the discharge curve of the model cell from **Figure 2a** were used as a reference. As the overpotential gradually increases, the discharge plateau shifts downwards (as indicated by the qualitative shift of the blue dashed line in **Figure 2a**). This allows us to determine the discharge plateau voltage (approximately the average voltage) and capacity for each overpotential. The corresponding energy output can be calculated using the formula in **Figure 2b**.

5. Measurements of Li^+ transport overpotential through modified separators

Li|Li symmetric cells (CR2032), consisting of a "Li|PP|membrane|PP|Li" structure, were used to investigate the overpotential of lithium-ion transfer through both the commercial PP separators (control cell) and various membrane-modified separators. The electrolyte consisted of a standard solution containing 1 M LiTFSI in DOL/DME (1:1, v/v). To prevent contact of the membranes with the lithium electrodes and unwanted lithiation reactions, the membranes were all sandwiched between two PP separators, while the control cell composed of only two bare PP separators.

6. Li^+ diffusion coefficient

Li|SS cells (CR2032), consisting of a "Li|PP|membrane|PP|SS" structure, were used to measure the Li^+ diffusion coefficient (D_{Li^+}, $cm^2\ s^{-1}$) of different membrane-modified separators. Each cell was injected with 60 μL of electrolyte (1 M LiTFSI in DOL/DME, 1:1 v/v) to adequately meet the Li^+ conduction requirements. Firstly, a fixed amount of 1 mAh Li-electroplating was performed on the SS plate using the Li|SS half cells. Then, the electroplated Li was electrostripped off from the SS plate at different scan rates using linear sweep voltammetry (LSV) method to obtain peak currents at different scan rates. It is worth noting that the D_{Li^+} measured here are the overall results of the half cells, which are dynamically affected by various factors during the electrochemical testing process, including the lithium foil condition, electrolyte condition, lithium deposition and stripping processes, solid-electrolyte interface formation, and membranes. Therefore, we would like to point out that it is inappropriate to solely consider D_{Li^+} as an inherent characteristic of the membrane or the separator itself, even though some studies did so. However, this test can be used to determine the effects of different membrane-modified separators on the diffusion of lithium ions in the batteries.

The LSV measurements were performed with seven sweeping rates, *i.e.*, 0.02, 0.04, 0.06, 0.08, 0.10, 0.12, and 0.14 mV s^{-1}, as shown in **Figure S15**. The D_{Li^+} was derived using the Randles–Sevcik equation as described below according to literature[2]:

$$I_P = 2.69 \times 10^5\ C\ mol^{-1}\ V^{-1/2} \cdot n^{3/2} \cdot A \cdot D_{Li}^{1/2} \cdot v^{1/2} \cdot C_{Li}$$

where I_p indicates the peak current (A), n is the number of electrons in the reaction (n=1 for Li electroplating/stripping processes), A is the electrode area (cm^2), v is the scanning rate (V s^{-1}), and C_{Li} is the Li^+ concentration in the electrolyte (0.001 mol cm^{-3}). Note that the constant with a value of 2.69×10^5 has units of C mol^{-1} $V^{-1/2}$. The linear relationship between the I_p and the square root of $v^{1/2}$ can be derived from CV measurements.

7. H-cell measurements

The entire testing process was carried out in an Ar-filled glovebox (H_2O < 0.1 ppm, O_2 < 0.1 ppm). The H-cell consists of two symmetrical containers that can be locked together in the middle using a spring clip. Prior to the test, the separators to be tested (either PP or modified separators) was sandwiched between two O-ring foot pads and locked in the middle of the H-cell. Next, 35 mL of 1.0 M Li_2S_8 catholyte, which contained 1.0 M lithium bis(trifluoromethanesulfonyl)imide (LiTFSI, 99.95%, Sigma Aldrich) and a 1:1 volume ratio of DOL/DME, was added to both sides of the H-cell. The Li_2S_8 catholyte was obtained by mixing Li_2S and S powder at a molar ratio of 1:7 and heating and stirring the mixture in a 1:1 volume ratio of DOL/DME for 12 hours, followed by dissolving LiTFSI to make it 1.0 M. The anode of the H-cell was a lithium foil (d=15 mm) held in place with a platinum metal clamp, and the cathode was an aluminum foil coated with porous

carbon (d=15 mm). A magnetic stirrer (1000 rpm) was placed on each side of the H-cell to reduce the impact of concentration polarization. The top covers of the H-cell were sealed with a Teflon tape to prevent evaporation of the catholyte. After each test, the H-cell was washed and dried, and a fresh catholyte was refilled for the next separator measurement.

The two electrodes of the H-cell were connected to the CHI660 tester outside the glovebox via feed-through cables. Galvanostatic discharge was used to record the discharge reaction points of the positive electrode, with each current being tested for 60 s. Since different membranes have different obstacles to Li^+ transport, membranes with a higher Li^+ impedance will cause a larger overpotential and shift the discharge plateau of the cathode to a lower voltage. By comparing the discharge potentials of the H-cell with modified separators and PP separator, the difference in overpotential at a certain current or C-rate can be calculated.

The testing current densities were calculated based on the assumed C-rates corresponding to a sulfur loading of 6mg cm^{-2} on the cathode of a Li–S battery. For example, in this study, C-rates of 0.02, 0.05, 0.1, 0.2, 0.5, and 1.0C during the discharge processes equal to 0.355 mA, 0.888 mA, 1.776 mA, 3.552 mA, 8.88 mA, and 17.76 mA.

8. Li_2S_6 permeation tests through different separators

Polysulfide permeation tests were conducted using an H-cell, comprising two identical glass containers. These containers can be hermetically sealed at the top and connected at the center via a clamp, encompassing an aperture of 15 mm. In a standard procedure, a separator (diameter approximately 28 mm) was positioned to entirely cover this aperture. After sealing, the membrane underwent a meticulous inspection to detect any potential cracks or unblocked openings. Subsequently, 25 mL of a 37.5 mM Li_2S_6 in DOL/DME (1:1 v/v) solvent was introduced into one side of the H-cell, and an equivalent volume of a blank solvent without any Li_2S_6 was added to the opposite side. The assembly was then placed on a level surface. Quantitative assessments of polysulfide diffusion through four separators—commercial PP, 050HG/PP, 030HG/PP, and rGO/PP, each with an equal mass of membrane materials—were performed. These evaluations involved polysulfide permeation tests and UV-vis analysis (Figure S16). The permeation process was continuously monitored by extracting 300 μL samples from the solution on the lower concentration side of the H-cell at 15-min intervals, repeating this process five times. To ensure that the absorbance readings fell within the accurate range (typically below 2) of the UV-vis spectrophotometer, the permeate solutions were diluted tenfold, and the final results were recalibrated by multiplying by a factor of 10. All solutions were handled in an argon-filled glovebox, and hermetically sealed before removal from the glovebox for UV-vis measurements.

9. Nyquist plots and Li^+ activation energies

Li^+ activation energies ($E_{a\text{-}Li^+}$) of commercial PP and modified separators were determined by Nyquist plots from the electrochemical impedance of stainless steel (SS)|SS symmetric cells, consisting of a "SS|PP|membrane|PP|SS" structure, featuring various membranes at multiple temperatures (*i.e.*, 10, 20, 30, 40, 50, 60°C).

The SS|SS symmetric cells were assembled in an Ar-filled glovebox. The membranes were sandwiched between two PP separators for electrical insulation from the SS plates. Each cell was injected with 60 μL of electrolyte (1M LiTFSI in DOL/DME, 1:1 v/v) to adequately meet the ionic

conduction requirements. Electrochemical impedance spectroscopy (EIS) was conducted within the frequency range of 1 MHz to 0.1 Hz. Before initiating the EIS tests, each cell was placed in a constant-temperature chamber via feed-through cables at finely controlled temperatures for at least 60 min to ensure good temperature uniformity within the cell, after which testing commenced, as exemplified in **Figure S20**. The value of $E_{a\text{-}Li^+}$ of each separator was derived from the slope of the fitted line in the Arrhenius plot.

10. Modeling of Li^+ transfer through membranes

The Li^+ mass transport simulation was performed using the Mass Transport Module of COMSOL Multiphysics 6.1. The mass transport model employed in this study was developed by optimizing and refining the frameworks established in our previous investigations.[1, 3, 4] The additional mass transfer mechanisms encompassed convection and mass transfer in porous media, where the concentration was treated as a linear function with electric field migration neglected.

Specifically, the mass transport model consisted of a Li|PP|Li or Li|PP|membrane|Li cell configuration, which aimed to simulate the temporal evolution of C_{Li^+} between two electrodes within the cell under ideal unidirectional current transmission conditions. In this model, the cell current density was set at 5.92 mA cm^{-2}, equivalent to the current density observed in a Li–S battery with a low sulfur loading of 2 mg cm^{-2} cycled at 1C rate. The employed electrolyte was a commercially available electrolyte, consisting of 1M $LiPF_6$ in a 1:1 ratio of EC:DEC. The electrolyte was considered non-solid, and its initial concentration in the model was set to 1.0 M, while temperature and pressure were set to the standard values provided by the software. Although COMSOL currently lacks a ready model for 1M LiTFSI in a 1:1 ratio of DOL:DME electrolyte specific to Li–S batteries, we opted to use the available electrolyte model as a reasonable approximation. The activity coefficient for Li^+ in the electrolyte (f_C) was adopted from published literature, with a value of 0.60.[5] The average value of the lithium ion diffusion coefficient (D_C) was determined as 6×10^{-10} m^2 s^{-1} and assumed to be isotropic based on literature.[5-7] The remaining physical properties of the electrolyte were set to default values within the software environment to ensure a consistent foundation for simulation parameters.

In this study, to improve simulation efficiency, a uniform thickness of 1 μm was assigned to the modification layer, while the PP separator remained at 25 μm. The upper and lower boundaries in the model corresponded to the stripping and deposition reactions of Li metal foils, with reaction rates of +6.14 mol m^{-2} s^{-1} and −6.14 mol m^{-2} s^{-1}, respectively, corresponding to the specified current density. Furthermore, no flux was present at the boundaries and within the model units of the PP separator and modification layers. In the modeling, graphene building blocks were set to have a thickness of 13 nm with an average vertical gap of 20 nm, so holes with a diameter greater than or equal to 13 nm were considered as effective Li^+ transport channels. Thus, the former has an effective hole ratio of 82.1%, and the latter has an effective hole ratio of 72.8%.

Additionally, it is worth noting that in previous simulation studies, researchers often failed to construct a reasonable model that recreates the hole size and structure. For instance, directly using the average hole size of 40–50 μm in the PP separator as the 2D dimension in modeling is incorrect, as it significantly overestimates (potentially by at least 5-6× as observed) the projected area ratio of Li^+ channels on the membrane cross-section. This leads to overly optimistic estimations in simulation results. This issue remains unresolved even when placing the 2D model into a polar coordinate system. Therefore, in this study, we redesigned the equivalent area corresponding to the

holes within the membranes to ensure that the proportion of available Li^+ channels on the membrane cross-section aligns with the actual projection area of holes in the PP separator and HG membranes.

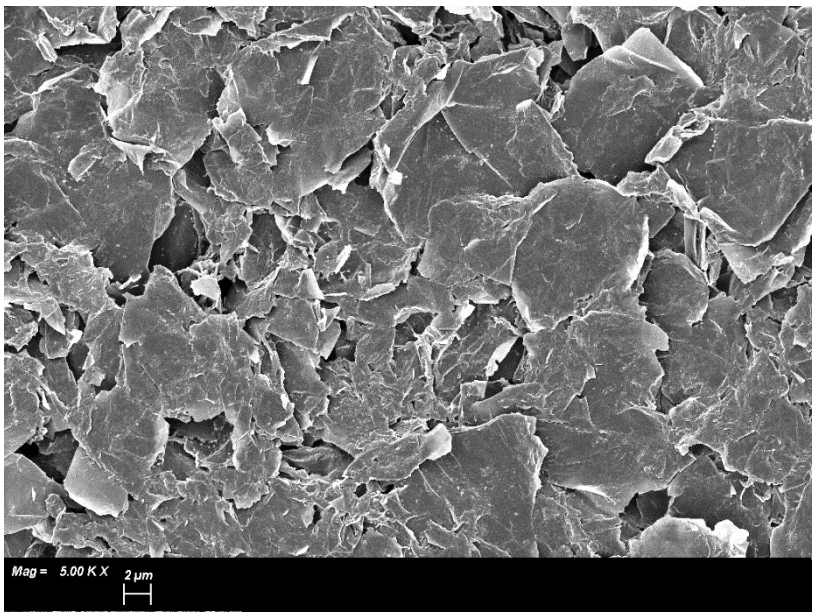

Figure S1. Top-view SEM image of rGO/PP separator. Pinholes and cracks were clearly observed across the surface of rGO/PP separator.

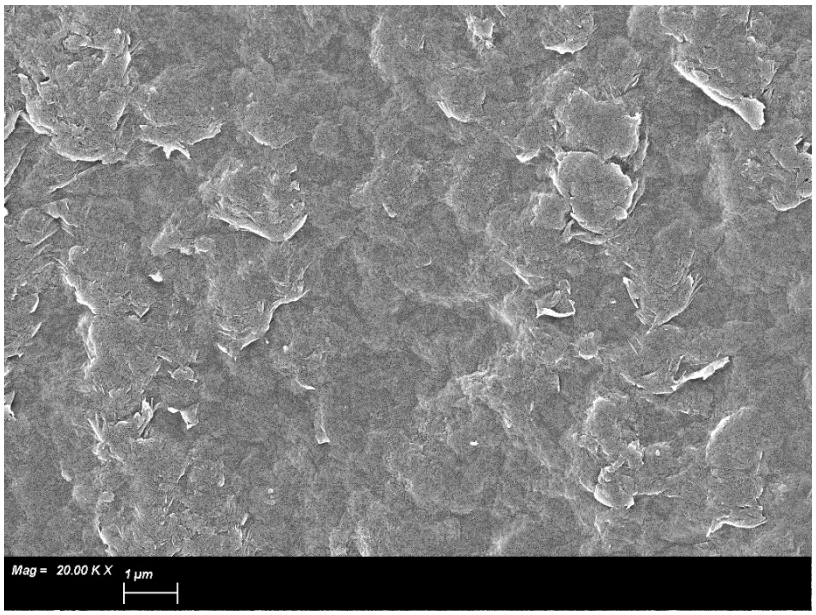

Figure S2. Top-view SEM image of GO/PP separator. No apparent pinholes or cracks were observed across the surface of GO/PP separator.

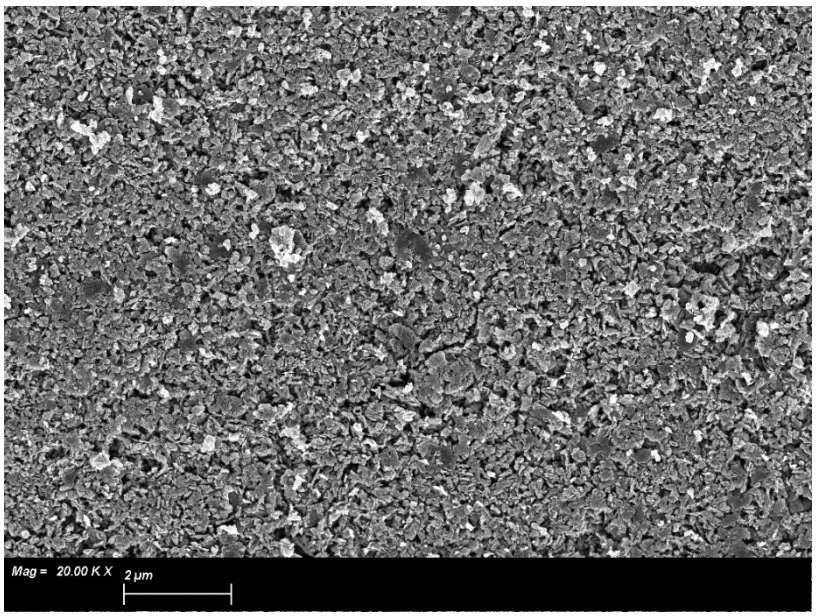

Figure S3. Top-view SEM image of $Co(OH)_2$/PP separator. Pinholes were clearly observed across the surface of $Co(OH)_2$/PP separator.

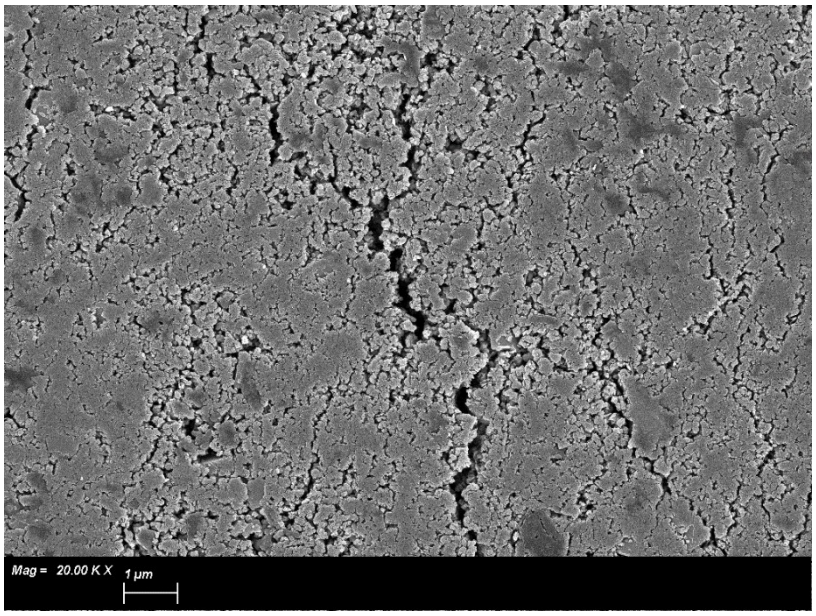

Figure S4. Top-view SEM image of SnS_2/PP separator. Obvious pinholes and cracks were observed across the surface of SnS_2/PP separator.

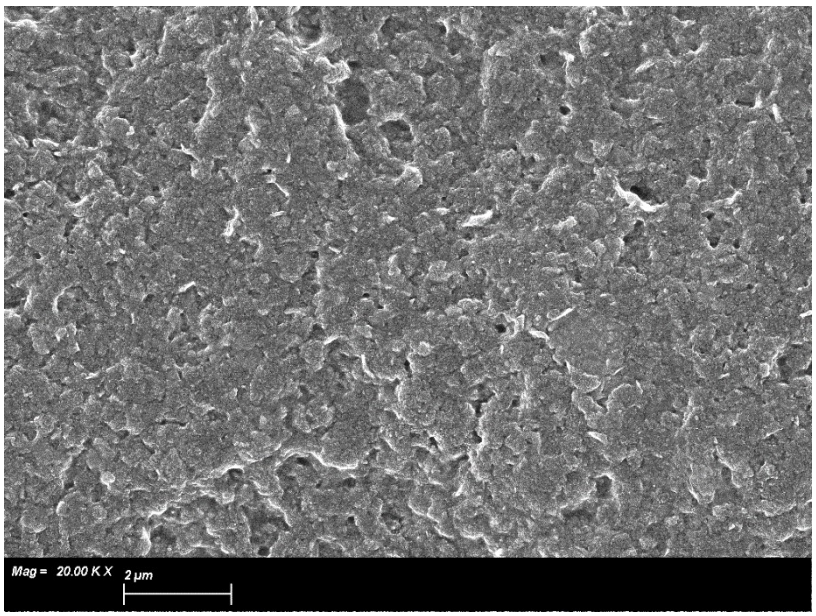

Figure S5. Top-view SEM image of MoS_2/PP separator. No apparent uncovered areas or cracks were observed across the surface of MoS_2/PP separator. Note that the darker regions are not holes, but shading caused by raised areas on the surface of the MoS_2 membrane.

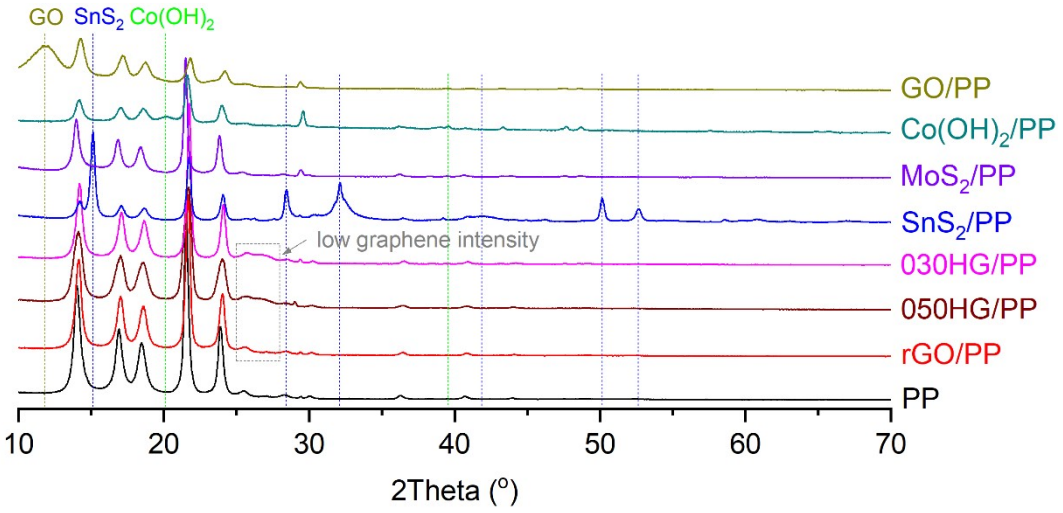

Figure S6. XRD results of commercial PP separator and various modified separators. The coating masses of all membranes are ~0.18 mg cm^{-2}.

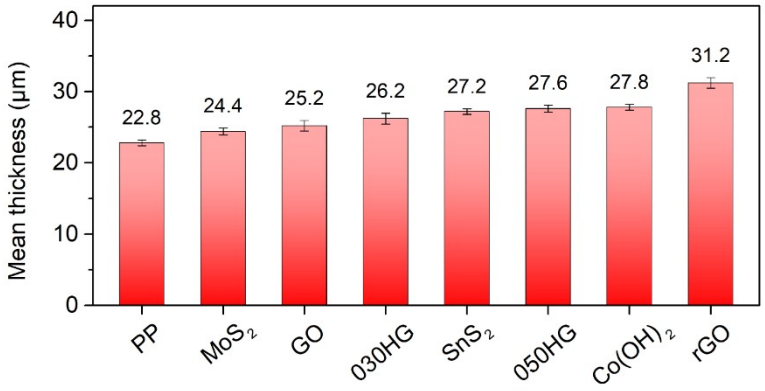

Figure S7. Measured thicknesses of commercial PP separator and various modified separators. Modified separators all have the same ~0.18 mg cm^{-2} loading of membrane materials.

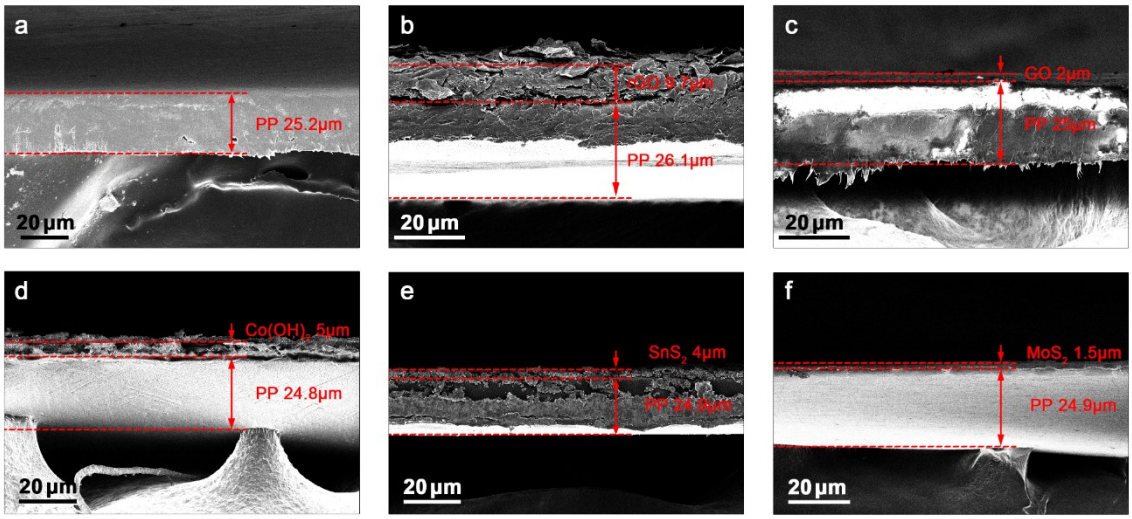

Figure S8. Cross-section SEM images of commercial PP and modified separators. Due to the extremely poor conductivity of PP separator itself, even after Pt coating, the uneven distribution of electronic conductivity in the separator results in overexposed areas in some SEM images.

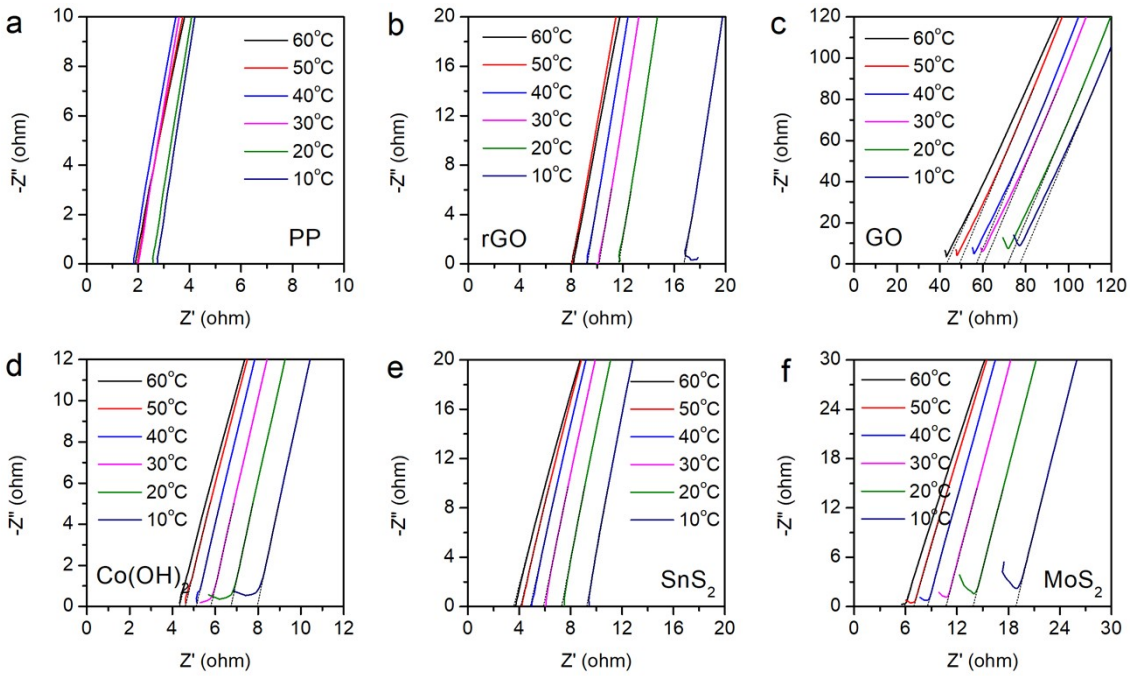

Figure S9. Electrochemical impedance spectroscopy (EIS) measurements performed at different temperatures for various separators.

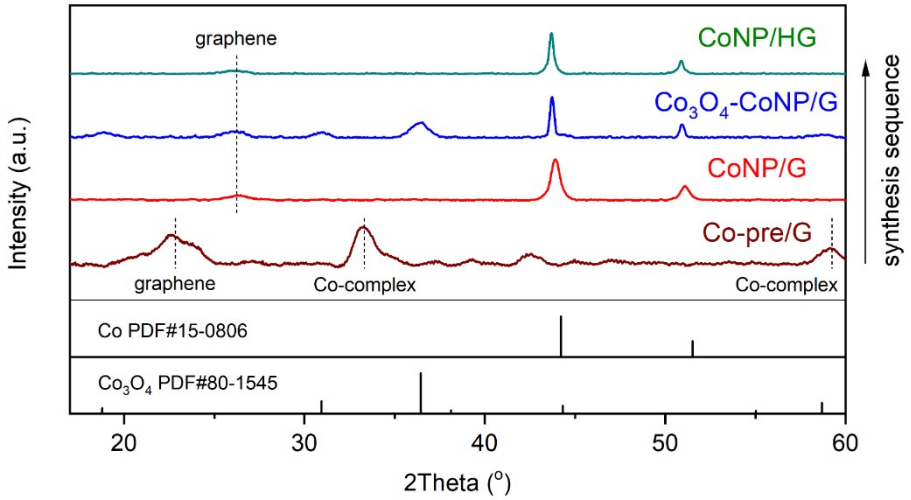

Figure S10. Synthesis sequence of HG before acid-treatment. The CoNP/HG obtained from the last step will be acid-treated using 8M hydrochloric acid solution at 60°C for at least 12 h to achieve the pure HG nanosheets.

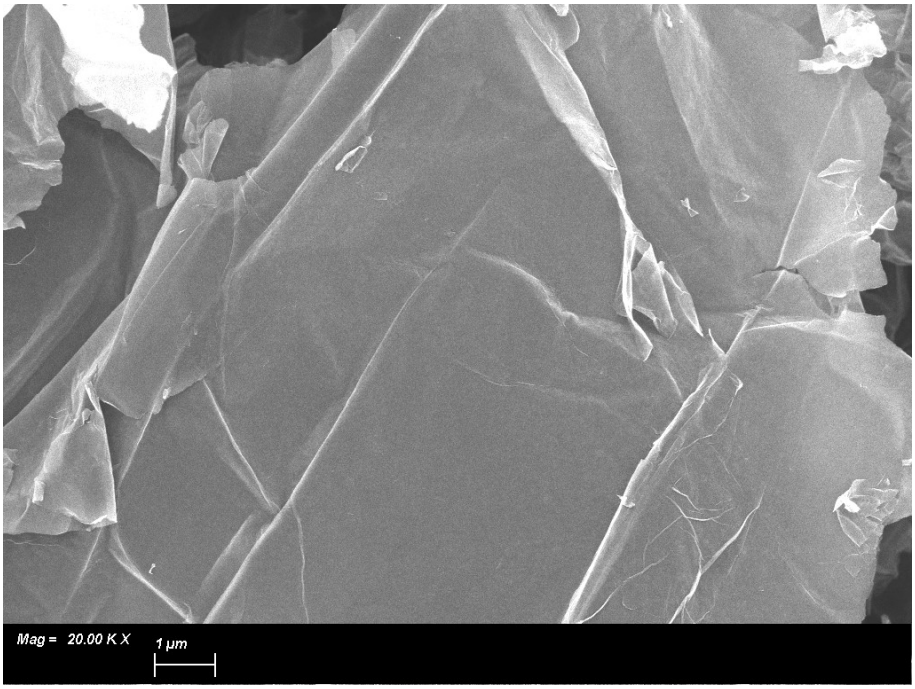

Figure S11. SEM image of Co-pre/G nanosheets.

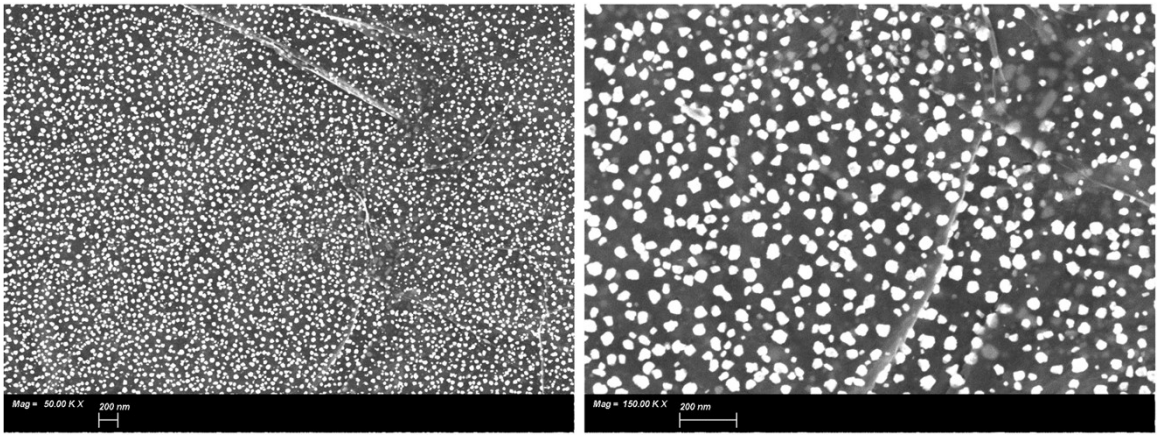

Figure S12. SEM image of CoNP/G nanosheets after annealed at 800°C in N_2. Note that at this stage of synthesis, the holes on graphene are not formed compared with Figure S13.

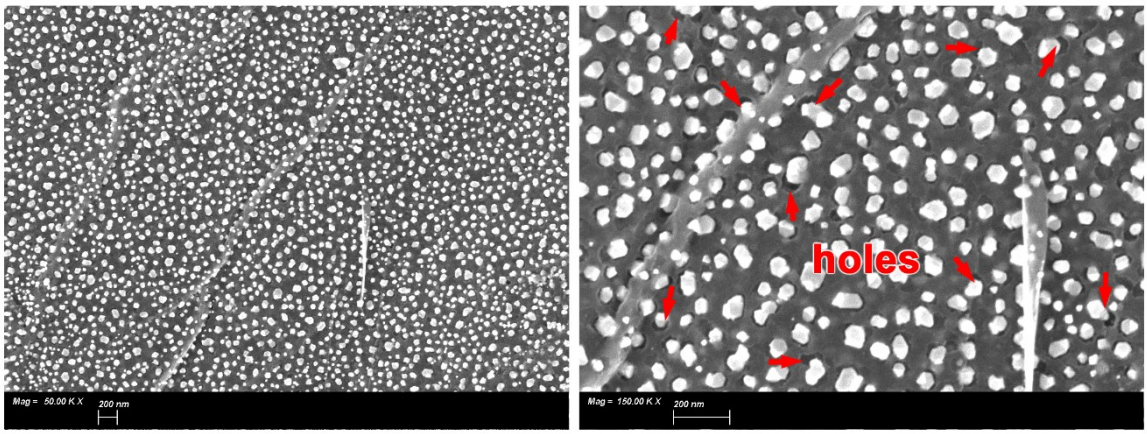

Figure S13. SEM images of CoNP/HG nanosheets after further annealing of the partially oxidized Co_3O_4-CoNP/G nanosheets at 800°C in N_2. Note that the holes on graphene (red arrows) began to reveal underneath the nanoparticles compared with Figure S12. This confirms that the holes are created by in-situ oxidation of graphene by the partially oxidized intermediate product Co_3O_4-Co nanoparticles, while the Co_3O_4 domains are carbothermically reduced to metallic Co at the same time.

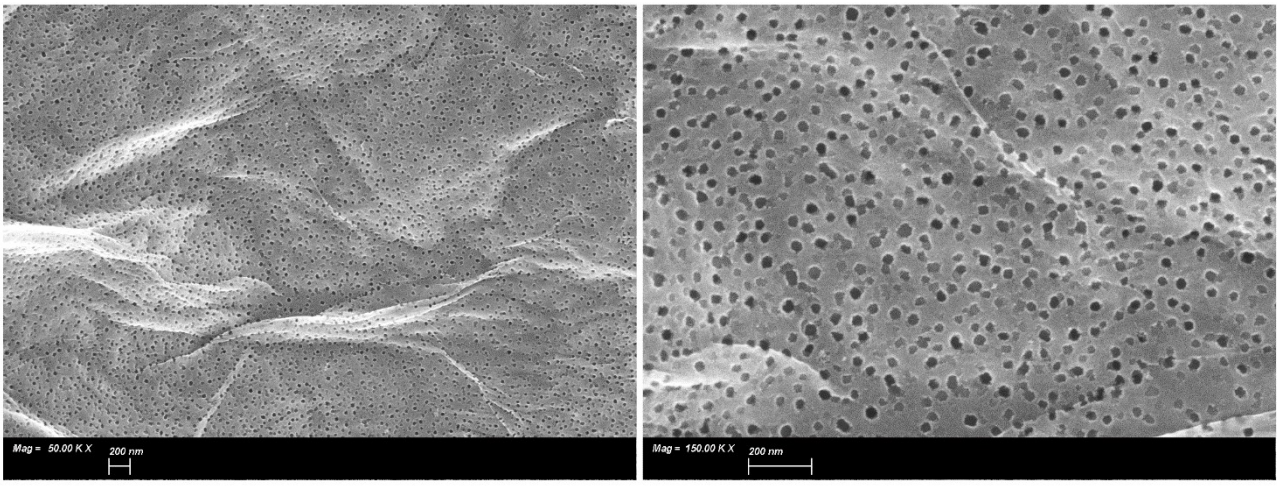

Figure S14. SEM images of 030HG nanosheets after acid-leaching.

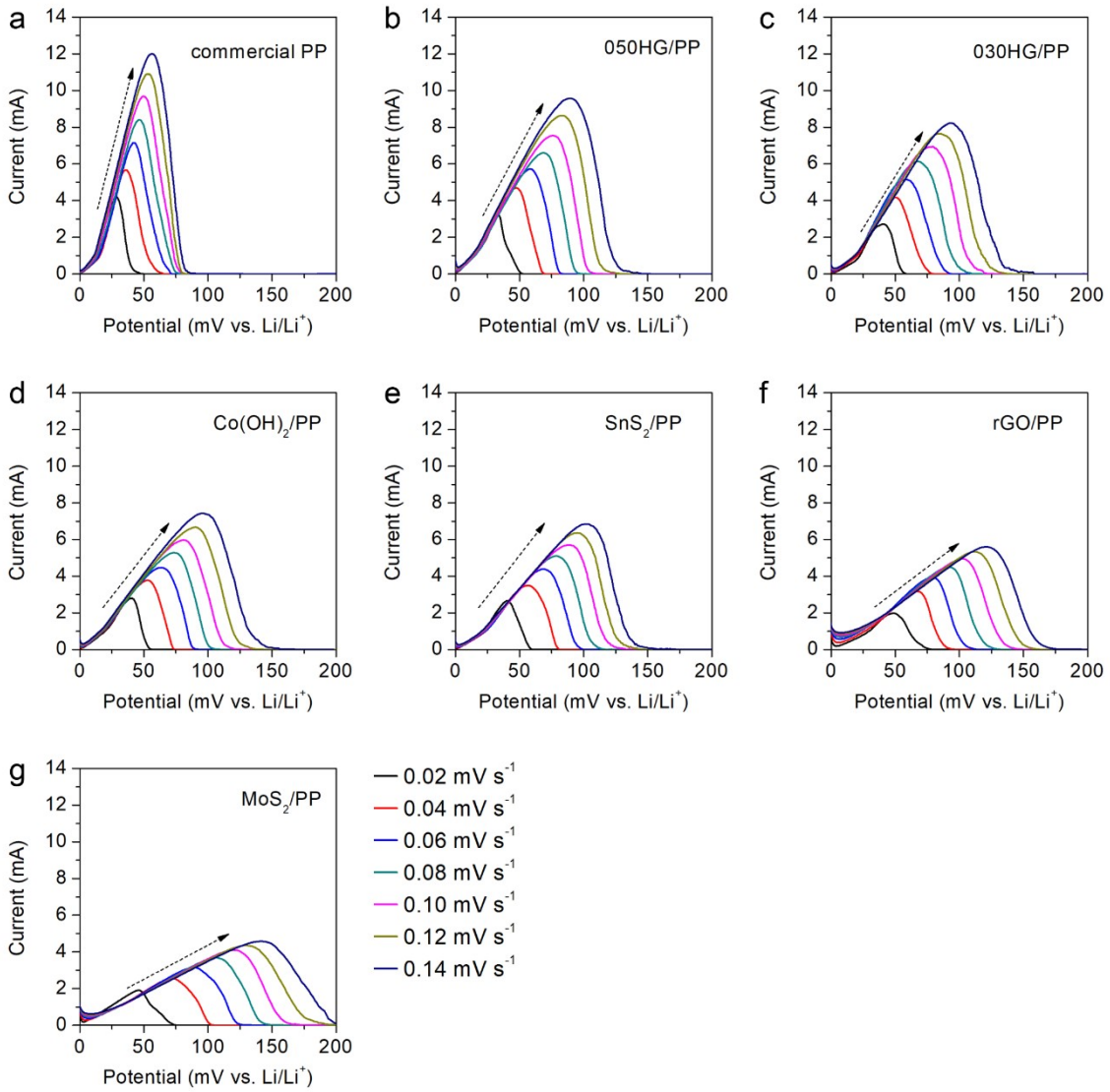

Figure S15. Linear sweep voltammetry (LSV) measurements performed at different sweeping rates for various separators.

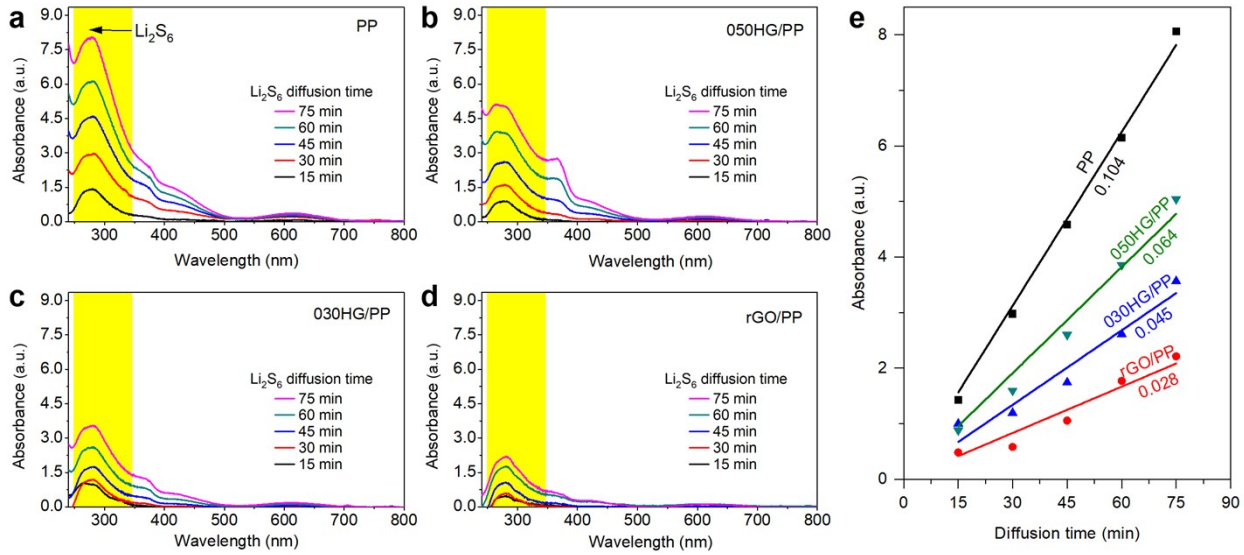

Figure S16. Soluble polysulfide (Li_2S_6) diffusion characterization through different separators in a H-cell. UV-vis absorbance of the clean solution during Li_2S_6 diffusion through the bare and membrane-modified separators: (a) PP, (b) 050HG/PP, (c) 030HG/PP, and (d) rGO/PP with the yellow highlighted area showing the wavelength absorption region of the polysulfides. (e) UV-vis absorbance peak values of Li_2S_6 at 280 nm as a function of the diffusion times for different separators. A larger slope of the fitted line indicates a higher Li_2S_6 diffusion rate through the membrane-modified and bare separators.

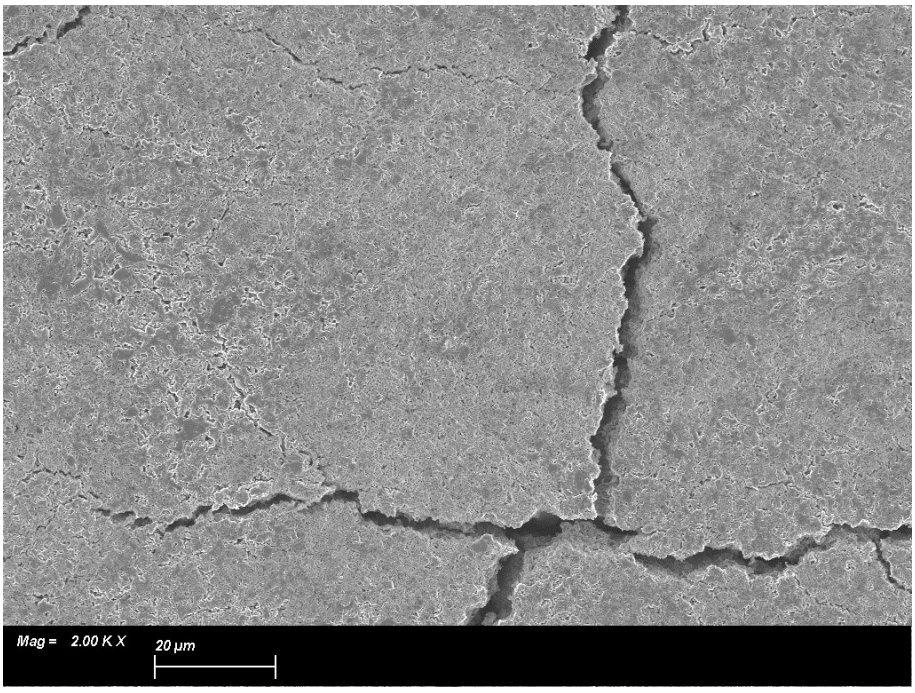

Figure S17. Surface morphology of Li foil after cycling with $Co(OH)_2$/PP separator. The surface of the lithium metal foil is covered with filaments, indicating that the Li^+ transport capability of the membrane in the battery is sufficient to fully utilize the lithium surface.

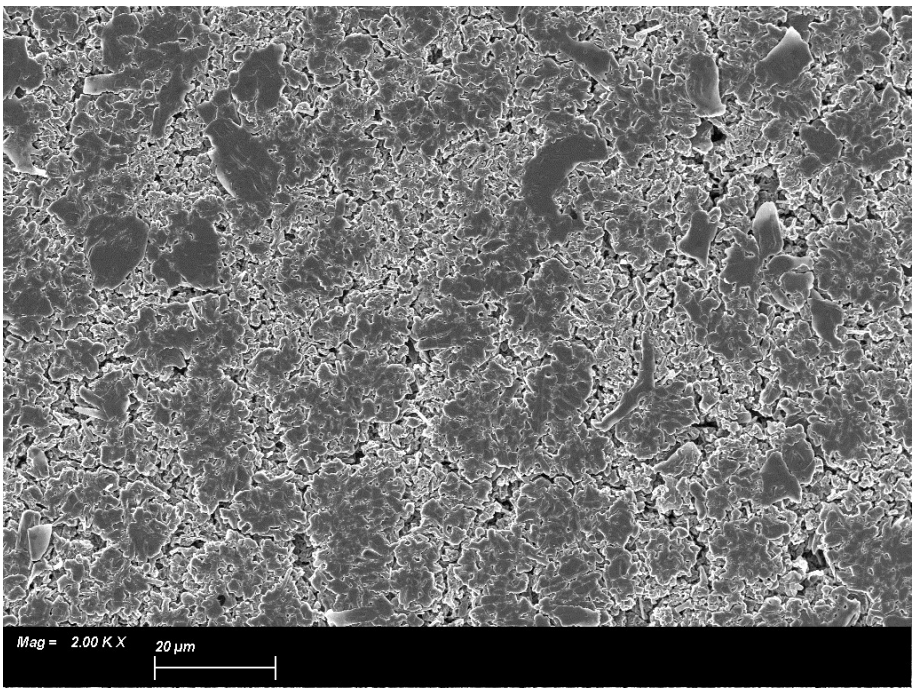

Figure S18. Surface morphology of Li foil after cycling with SnS_2/PP separator. The surface of the lithium metal foil is covered with filaments, indicating that the Li^+ transport capability of the membrane in the battery is sufficient to fully utilize the lithium surface.

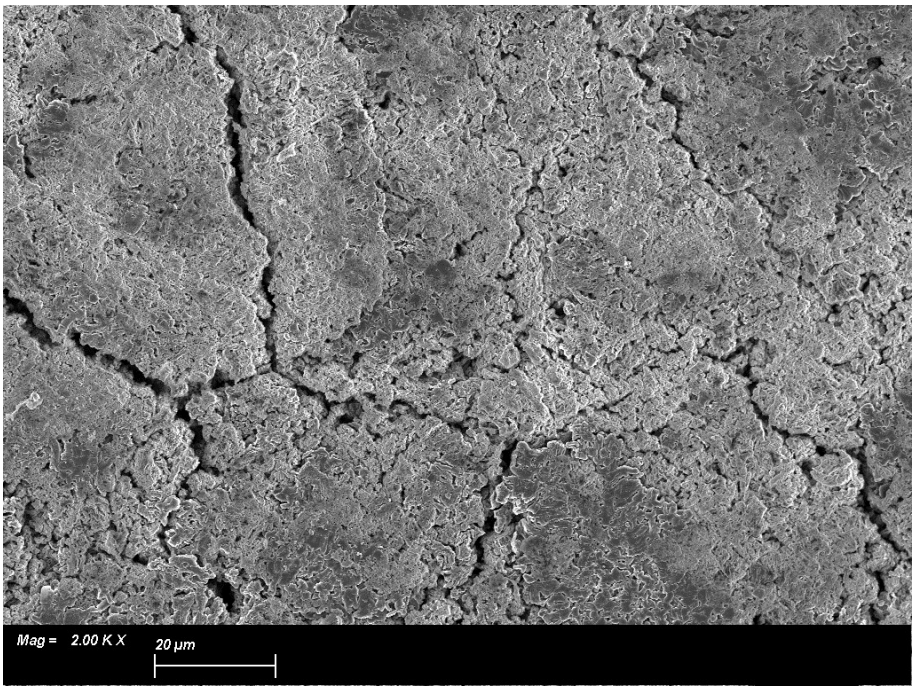

Figure S19. Surface morphology of Li foil after cycling with rGO/PP separator. The surface of the lithium metal foil is covered with filaments, indicating that the Li^+ transport capability of the membrane in the battery is sufficient to fully utilize the lithium surface.

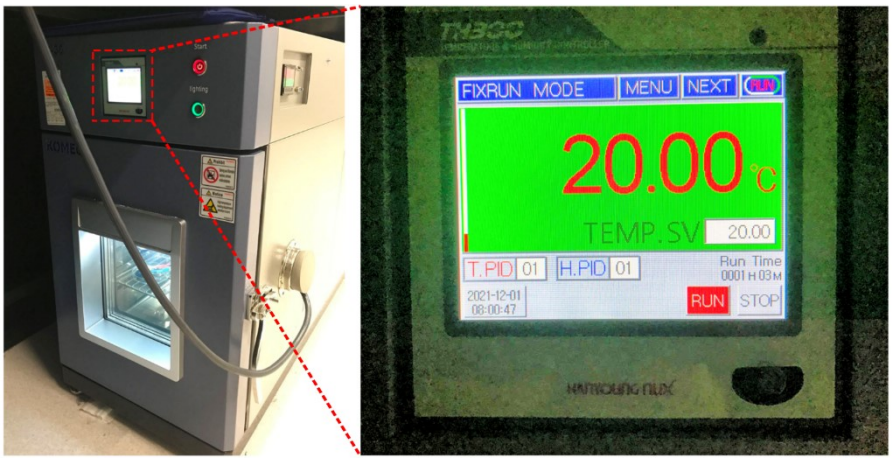

Figure S20. Constant-temperature chamber for temperature-dependent EIS tests.

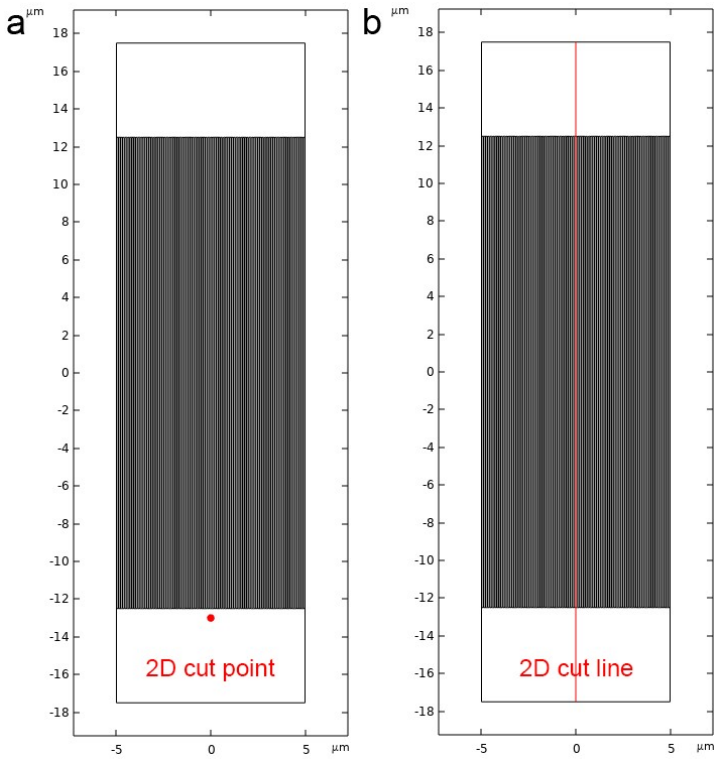

Figure S21. Data observation (control points) and collection method in modeling: (a) 2D cut point positioned 0.5 μm below the PP separator. (b) 2D cut line traversing the entire cell.

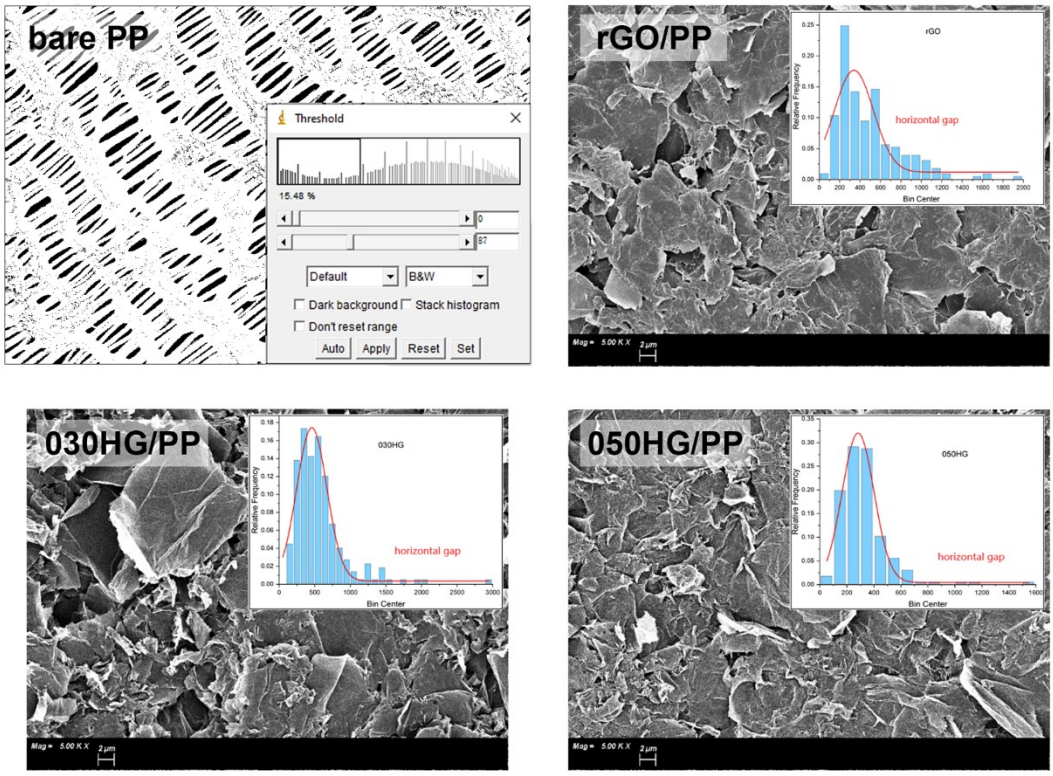

Figure S22. Statistical analysis of the pore area percentage of commercial PP separators and gap number and size between graphene nanosheets in the three types of modified separators.

References

1. B. Liu, J. F. Torres, M. Taheri, P. Xiong, T. Lu, J. Zhu, Y. Liu, G. Yu and A. Tricoli, *Advanced Energy Materials*, 2022, **12**, 2103444.
2. G. Zhou, H. Tian, Y. Jin, X. Tao, B. Liu, R. Zhang, Z. W. Seh, D. Zhuo, Y. Liu, J. Sun, J. Zhao, C. Zu, D. S. Wu, Q. Zhang and Y. Cui, *Proceedings of the National Academy of Sciences*, 2017, **114**, 840-845.
3. B. Liu, M. Taheri, J. F. Torres, Z. Fusco, T. Lu, Y. Liu, T. Tsuzuki, G. Yu and A. Tricoli, *ACS Nano*, 2020, **14**, 13852-13864.
4. J. F. Torres, A. Komiya, D. Henry and S. Maruyama, *The Journal of Chemical Physics*, 2013, **139**, 074203.
5. E. R. Logan, K. L. Gering, X. Ma and J. Dahn, *The Electrochemical Society Interface*, 2019, **28**, 49.
6. L. O. Valøen and J. N. Reimers, *Journal of The Electrochemical Society*, 2005, **152**, A882.
7. T. Nishida, K. Nishikawa and Y. Fukunaka, *ECS Transactions*, 2008, **6**, 1.
8. J. He, Y. Chen and A. Manthiram, *iScience*, 2018, **4**, 36-43.